Journal of Applied Fluid Mechanics, Vol. 17, No. 9, pp. 1885-1895, 2024.
Available online at www.jafmonline.net, ISSN 1735-3572, EISSN 1735-3645.
https://doi.org/10.47176/jafm.17.9.2595

Numerical Study on the Sloshing Behaviors of Dual Liquid Tanks with Gas Inflow

Y. F. Chen[1], C. Huang[1,2], W. H. Yan[1], G. P. He[1] and S. X. Zhang[3†]

[1] *School of Mechanical and Materials Engineering, North China University of Technology, Beijing 100144, China*
[2] *Ecole Polytechnique Montreal, Montreal, QC, Canada*
[3] *School of Civil Engineering, Shijiazhuang Tiedao University, Hebei 050043, China*

†*Corresponding Author Email: zhangsx@stdu.edu.cn*

ABSTRACT

The finite volume method (FVM) is used to numerically investigate the sloshing behaviors of dual liquid tanks with gas inflow in this study. The sloshing process of a single liquid tank is simulated to verify the feasibility of the numerical method. Three different inlet boundary conditions are then discussed in order to obtain a reasonable gas flow rate. The sloshing process of a dual liquid tank with the gas inflow is simulated, and the effects of three different factors on the sloshing behaviors are investigated. The results indicate that the overload, flow rate, and filling ratio can affect the peak value of the impact force acting on the tank wall. The impact force is positively proportional to the overload (1G, 3G, or 5G). An increase in flow rate (50 g/s, 1000 g/s, or 5000 g/s) or a decrease in filling ratio (99.52%, 75.64%, or 63.69%) can increase the size and number of bubbles, leading to intensified sloshing behavior and increased impact force.

Article History

Received January 17, 2024
Revised March 24, 2024
Accepted March 25, 2024
Available online July 2, 2024

Keywords:

Dual liquid tank
Finite volume method (FVM)
Gas inflow
Liquid tank sloshing
Multiphase flows

1. INTRODUCTION

The sloshing behavior of liquid tanks is common in the aerospace, marine, petrochemical, and other industries, such as liquid propellants in aircraft, liquid-carrying cargo ships, and tanker trucks. In particular, rocket engines in the aerospace field gradually tend toward a large thrust and high specific impulse, which cause intense sloshing behaviors in the tank. Liquid hydrogen and liquid oxygen cryogenic propellants are widely used in newly launched vehicles (Huang et al., 2020; Baek et al., 2022). Because the cryogenic propellant in the tank is generally pressurized by helium to maintain the inlet pressure of the pump, the liquid hydrogen in the tank is chronically supercooled, whereas the gas pillow area in the tank is overheated (Li, 2006; Wang et al., 2018; Li et al., 2023). During vehicle takeoff, flight, and landing, the cryogenic propellant in the tank produces strong sloshing under external excitation (Liu, 2011), thereby causing a large impact force to act on the tank. If there are no further reasonable pressurization measures, the engine thrust may drop, or the pump may form a broken flow, which would cause the engine to malfunction. To ensure safe engine operation, it is necessary to study the hydrodynamics of sloshing with a gas inflow.

The theoretical study of liquid tank sloshing is mainly based on the linear potential flow theory (Li et al., 2012; Brown et al., 2020; Ji, 2023) and equivalent mechanical models (Morais et al., 2020; Tsao et al., 2022; Chen et al., 2023). These theoretical methods usually do not consider the liquid viscosity and have some limitations in the study of sloshing with a large amplitude. In addition, these methods have certain requirements regarding the profiles and sizes of the liquid tanks. When sloshing is intense, the free surface becomes turbulent and fragmented (Bai, 2020; Yu, 2021), making it impossible for theoretical methods to solve the free surface fragmentation. Compare with theoretical methods, experimental methods are more intuitive and accurate, and experiments can provide reliable comparison results for validating theoretical and numerical methods. However, experimental methods are often limited by sites and measurement techniques, and they can be time-consuming, labor-intensive, and lengthy.

With improvements in computer technology, numerical methods have been applied to fluid mechanics to effectively solve complex flows. Popular numerical methods include the finite difference method (FDM) (Dong, 2002; Huang et al., 2003), finite element method (FEM) (Dong, 2002; Zhuang et al., 2006), boundary element method (BEM) (Dong, 2002; Kutlu et al., 2017;

Yao et al., 2017), finite volume method (FVM) (Dong, 2002; Huang et al., 2003; Hejranfar & Azampour, 2016; Koca & Zabun, 2021; Wan, 2021), and smoothed particle hydrodynamics method (SPH) (Shao et al., 2012; He et al., 2022; Zhang et al., 2023b). Saghi (2018) investigated the interactions between waves and tanks using the FDM and found that sloshing can enhance the motion of the tank. Shao et al. (2012) proposed an improved SPH method to model liquid sloshing, which provided a good prediction of wave height. Zhang et al. (2019) used a hybrid approach of improved SPH and SPEM to model fluid-structure interaction problems, which can effectively model FSI problems with large fluid deformations. Zhang et al. (2023a) used the FVM method with overlapping grid technology to simulate liquid sloshing, and their numerical results agreed well with experimental results.

At present, numerical research on sloshing mostly focuses on the airtightness, impact force, and stability of the liquid but less on sloshing with gas inflow. However, engineering practice still requires a further understanding of sloshing behavior with gas inflow. With an increase in the voyage demand, the sloshing of the liquid in the tank also exhibit transient characteristics. In this case, the additional moments and shock loads caused by sloshing may lead to the serious destruction of the structure. Therefore, it is necessary to understand sloshing behavior with gas inflow. In this study, the finite volume method (FVM) is adopted to simulate sloshing behavior with gas inflow. The effects of the overload, outlet flow, and filling ratio on the impact force and flow characteristics are discussed in detail.

2. NUMERICAL METHODS

The fluid used in this study is incompressible, and the sloshing behavior with the gas inflow is unsteady. The continuity and momentum equations in the Euler coordinate system are expressed as follows:

$$\frac{\partial \rho}{\partial t}+\rho\frac{\partial u_i}{\partial x_i}=0 \tag{1}$$

$$\rho\left[\frac{\partial u_i}{\partial t}+\frac{\partial (u_i u_j)}{\partial x_j}\right]=-\frac{\partial p}{\partial x_i}+\mu\frac{\partial}{\partial x_j}\left(\frac{\partial u_i}{\partial x_j}-\rho\overline{u_i' u_j'}\right)+\rho G_i \tag{2}$$

where ρ is the fluid density, t is the time, u_i and u_j are the time-averages of the velocity components, x_i and x_j are the spatial coordinate components, p is the time-average of the pressure, μ is the dynamic viscosity coefficient, G_i is the acceleration component of gravity, and $-\rho\overline{u_i' u_j'}$ is the Reynolds stress term.

The chosen turbulence model is the SST k-ω model proposed by Menter (Zhou et al., 2010), which is used to solve for the Reynolds stress term. The SST k-ω model is suitable for use with near-wall flow at low Reynolds numbers. The SST k-ω model applies this equation of the original k-ω model near the wall and that of the k-ε model away from the wall (Zeng et al., 2023). Therefore, the SST k-ω model can accurately predict the flow near the wall and improve the accuracy of the results, which is critical for accurately simulating the interaction between the fluid and the wall. The equations of the turbulent kinetic energy (k) and dissipation rate (ω) are presented below:

$$\rho\left[\frac{\partial k}{\partial t}+\frac{\partial (u_j k)}{\partial x_j}\right]=P_k-\rho C_\mu k\omega+\frac{\partial}{\partial x_j}\left[(\mu+\sigma_k\mu_t)\frac{\partial k}{\partial x_j}\right] \tag{3}$$

$$\rho\left[\frac{\partial \omega}{\partial t}+\frac{\partial (u_j \omega)}{\partial x_j}\right]=\frac{\gamma}{v_t}P_k-\beta\rho\omega^2+\frac{\partial}{\partial x_j}\left[(\mu+\sigma_\omega\mu_t)\frac{\partial \omega}{\partial x_j}\right]+2(1-F_1)\sigma_{\omega 2}\frac{\rho}{\omega}\frac{\partial k}{\partial x_j}\frac{\partial \omega}{\partial x_j} \tag{4}$$

where P_k is the average work of the fluid resisting the Reynolds stress (i.e., the turbulent kinetic energy production term), μ is the dynamic viscosity, μ_t is the eddy viscosity, v_t is the kinematic viscosity, and $C_\mu = 0.09$ is a constant. σ_k, γ, β, and σ_ω are solved by:

$$\varphi=\mathrm{F}_1\varphi_1+(1-\mathrm{F}_1)\varphi_2 \tag{5}$$

where φ represents σ_k, σ_ω, β, and γ in the SST model. φ is solved by the parameters φ_1, φ_2, and F_1. φ_1 is the parameter in the original k-ω model that can represent σ_{k1}, $\sigma_{\omega 1}$, β_1, and γ_1, whereas φ_2 is the parameter in the standard k-ε model that can represent σ_{k2}, $\sigma_{\omega 2}$, β_2, and γ_2. These parameter values are obtained by the following: σ_{k1} =0.85, $\sigma_{\omega 1}$ =0.5, β_1 =0.075, $\gamma_1=\frac{\beta_1}{C_\mu}-\frac{\sigma_{\omega 1}\lambda^2}{\sqrt{C_\mu}}$, σ_{k2}=1.0, $\sigma_{\omega 2}$ =0.856, β_2=0.0828, $\gamma_2=\frac{\beta_2}{C_\mu}-\frac{\sigma_{\omega 2}\lambda^2}{\sqrt{C_\mu}}$, where λ =0.41.The hybrid function F_1 is designed to enable the prediction of turbulent flow near the wall using the k-ω model and capture of free flow away from the wall using the k-ε model. The hybrid function F_1 is solved using the following equations:

$$F_1=tanh(arg_1^4) \tag{6}$$

$$arg_1=min\left[max\left(\frac{\sqrt{k}}{0.009\omega y},\frac{500v}{y^2\omega}\right),\frac{4\rho\sigma_{\omega 2}k}{CD_{k\omega}y^2}\right] \tag{7}$$

$$CD_{k\omega}=max\left(2\rho\sigma_{\omega 2}\frac{1}{\omega}\frac{\partial k}{\partial x_j}\frac{\partial \omega}{\partial x_j},10^{-20}\right) \tag{8}$$

where y is the minimum distance to the wall and v is the kinematic viscosity coefficient.

The turbulent kinetic energy production term (P_k) in Eqs. (3) and (4) can be computed as follows:

$$\mathrm{P_k}=\tau_{\mathrm{ij}}\frac{\partial \mathrm{u_i}}{\partial \mathrm{x_j}} \tag{9}$$

where

$$\tau_{\mathrm{ij}}=-\rho\overline{\mathrm{u_i'u_j'}}=\mu_{\mathrm{t}}\left(2\mathrm{S_{ij}}-\frac{2}{3}\frac{\partial \mathrm{u_k}}{\partial \mathrm{x_k}}\delta_{\mathrm{ij}}\right)-\frac{2}{3}\rho\mathrm{k}\delta_{\mathrm{ij}} \tag{10}$$

$$\mathrm{S_{ij}}=\frac{1}{2}\left(\frac{\partial \mathrm{u_i}}{\partial \mathrm{x_j}}+\frac{\partial \mathrm{u_j}}{\partial \mathrm{x_i}}\right) \tag{11}$$

where τ_{ij} is the Reynolds stress and δ_{ij} is the Kronecker symbol.

The eddy viscosity (μ_t) in Eqs. (3) and (4) are calculated as follows:

$$\mu_t=\rho\frac{\alpha_1 k}{max(\alpha_1\omega,\Omega F_2)} \tag{12}$$

$$v_t=\frac{\mu_t}{\rho} \tag{13}$$

$$\Omega=\sqrt{2\Omega_{ij}\Omega_{ij}},\Omega_{ij}=\frac{1}{2}\left(\frac{\partial u_i}{\partial x_j}-\frac{\partial u_j}{\partial x_i}\right) \tag{14}$$

where $\alpha_1 = 0.31$ is the structural parameter, F_2 is the boundary layer hybrid function, and Ω is the vorticity. The hybrid function F_2 is solved using the following equations:

$$F_2 = tanh(arg_2^2) \tag{15}$$

$$arg_2 = max\left(\frac{2\sqrt{k}}{0.009\omega y}, \frac{500v}{y^2\omega}\right) \tag{16}$$

The volume-of-fluid (VOF) method is used to compute the volume fractions of gas and liquid in each mesh to track the two-phase interface. The interface position is determined by the volume fraction of the phase. The volume fraction of the phase in a mesh cell can be determined by

$$\begin{cases} \theta_w = 0, \text{gas} \\ 0 < \theta_w < 1, \text{free surface} \\ \theta_w = 1, \text{liquid} \end{cases} \tag{17}$$

where θ_w is the liquid volume fraction. The relational expressions of density (ρ) and the kinetic viscosity coefficient (ε) for the two-phase flow are as follows:

$$\rho = \theta\rho_w + (1-\theta)\rho_a \tag{18}$$

$$\varepsilon = \theta\mu_w + (1-\theta)\mu_a \tag{19}$$

where the subscripts w and a denote liquid and gas, respectively. The interface between the gas phase and liquid phase is denoted by θ=0.5.

Based on the commercial software ANSYS Fluent (Wang, 2016), FVM is used to simulate the sloshing of the tank. A pressure-based solver is selected for this study. For complex boundary conditions, this solver is more stable than the other solvers, and its efficiency tended to increase as the mesh quality increased. The PISO algorithm is selected as the solution. The Green-Gauss cell method is used to calculate the gradient term, whereas the PRESTO! format is used to discretize the pressure term. The second-order upwind format is used for momentum. Finally, a bounded second-order implicit format is selected to discretize the time term.

3. The Sloshing Of A Single Liquid Tank And Discussions Of Inlet Boundary Conditions

3.1 Sloshing of a Single Liquid Tank

To verify the numerical method, this study simulate the sloshing process of a single liquid tank by He et al. (2022). As shown in Fig. 1, the length L and height H of the closed rectangular tank are 1.3 m and 0.9 m, respectively. The tank is partially filled with water; the depth of the water is d=0.2, and the height of the domain is H=0.8 m. The tank underwent sinusoidal motion in the horizontal direction as follows:

$$a = Asin(\omega t) \tag{20}$$

where A and ω are the overload acceleration and angular frequency of the sinusoidal motion, respectively. In this case, the overload acceleration A is 0.1 G (where G represents the gravitational acceleration), and the angular frequency ω is 3.11 rad/s. The density of water is

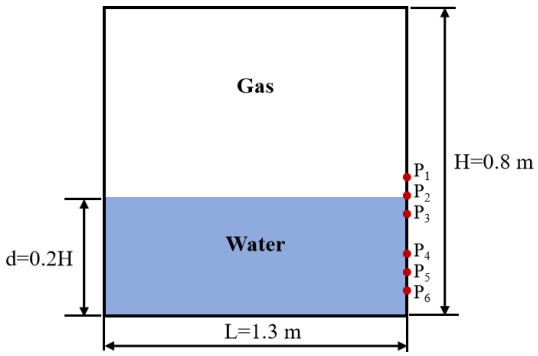

Fig. 1 Computational model of a single liquid tank

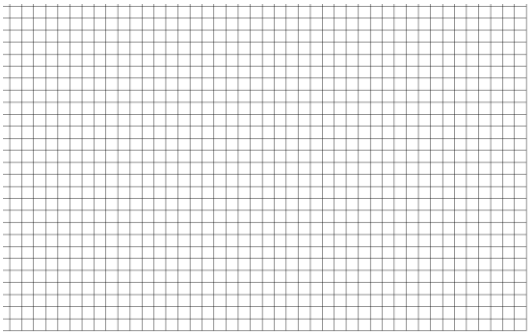

Fig. 2 Schematic diagram of the local meshes near the bottom boundary

ρ_w=1000 kg/m^3, the density of air is ρ_a=1 kg/m^3, and a background pressure of p_{back}=500 Pa is introduced into the simulations. The ratio of the dynamic viscosity coefficients of water and air is set to μ_w/μ_a=40, and the dynamic viscosity coefficient of water is μ_w=0.001 kg/(m·s). For the unsteady-state simulations, the simulation parameters remain constant over time. The time step is 0.001 s, and this value is held constant throughout the computational domain. Monitoring points are set on the right side of the tank to monitor the impact force acting on the tank wall. As shown in Fig. 1, there are six monitoring points: P_1, P_2, P_3, P_4, P_5, and P_6. These monitoring points are located at 0.195, 0.180, 0.165, 0.135, 0.120, and 0.105 m from the bottom, respectively.

A mesh-independent verification must be performed before the calculation to ensure the accuracy of the calculation. A uniformly distributed structural mesh is adopted to simulate a single liquid tank. Figure 2 shows a schematic of the local mesh. As listed in Table 1, three different meshes are considered for mesh-independent verification. The cell sizes Δ of the three different meshes are 12, 6, and 3 mm, respectively. The corresponding maximum aspect ratios are 1.0355, 1.0411, and 1.3353, and the corresponding maximum skewness values are 0.024951, 0.031352, and 0.45507, respectively. The calculation times consumed by the three meshes are 15720, 13980, and 18960 s, respectively.

Figure 3 shows the distributions of the liquid and gas at different moments. From left to right, the results are simulated by FVM with cell sizes of 12, 6, and 3 mm,

Table 1 Cell sizes and node numbers for three different meshes

Δ (cell sizes)	Node numbers	Maximum aspect ratio	Maximum skewness	Required calculation time (s)
12 mm	8284	1.0355	0.024951	13980
6 mm	32918	1.0411	0.031352	15720
3 mm	130640	1.3353	0.45507	18960

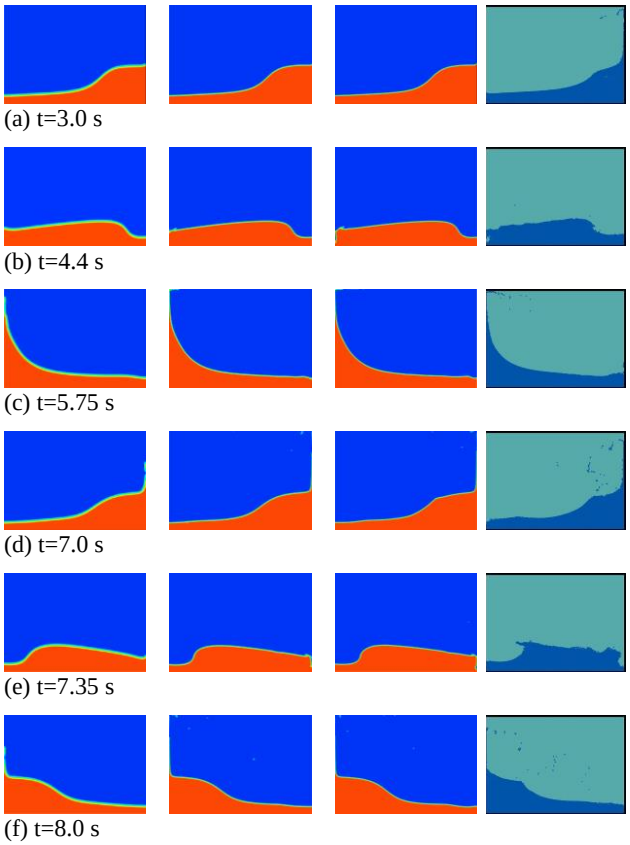

Fig. 3 Distributions of the liquid (red) and gas (blue) at different moments: (a) t=3.0 s, (b) t=4.4 s, (c) t=5.75 s, (d) t=7.0 s, (e) t=7.35 s, and (f) t=8.0 s. From left to right: FVM results with Δ=12 mm, FVM results with Δ=6 mm, FVM results with Δ=3 mm, and SPH results (He et al., 2022)

respectively, and compared with the results of the SPH method. The liquid strongly impacts the liquid tank, leading to a large deformation and splashing. The multiphase interface is well-maintained, even when splashing occurred. With an increase in mesh resolution, the details of the free surface became clearer. Both the FVM and SPH methods provide reasonable predictions. Obvious wave breaking and splashing can be observed in the SPH method, whereas the free surface obtained by the FVM is smoother. Although the free surface predicted by the SPH method is more violent, the FVM results are close to the SPH results.

Figure 4 shows the free surface profiles calculated using FVM and SPH. Over time, the free surface profiles of the mesh with a cell size of 12 mm differ from those computed using the other two meshes. In general, the free-surface profiles obtained via FVM are consistent with the SPH results. Moreover, smaller cell sizes can yield results closer to those obtained using SPH. Figure 5 shows the pressure of the monitoring points versus time using FVM, SPH, and experimental data. SPH tends to predict a smaller peak pressure, whereas FVM tends to predict larger values; however, both results are close to the experimental results. In addition, as the resolution of the meshes increase, the peak pressure values tend to remain consistent.

Therefore, the above results prove that the current numerical method is capable of simulating the sloshing behavior of a tank and predicting the profiles of the free surface and impact force acting on the tank wall. Furthermore, numerical convergence is achieved at a mesh spacing of 6 mm. To improve computational efficiency and maintain computational accuracy, a mesh with a cell size of 6 mm is selected for subsequent numerical simulations.

3.2 Discussion of Inlet Boundary Condition

3.2.1 Computational Model and Parameters

The selection of the inlet is essential for maintaining the safety of the engine and stability of the computing process. To obtain reasonable inlet boundary conditions, it is necessary to investigate the effect of the inlet boundary conditions on the numerical results. Figure 6 shows the computational model. The gas flowed into the tank from the inlet, which is located in the upper-right corner of the tank, and the liquid flowed out of the tank from the outlet, which is located in the lower-left corner of the tank. The dimensions of the inlet and outlet are both 0.01 m. The initial height of the liquid surface is 0.053 m. The density, dynamic viscosity, and background pressure are identical to those described in Section 3.1. Sinusoidal motion is expressed using Eq. (20), where the overload acceleration A is 1G and the angular frequency ω is 6.28 rad/s. In this case, the flow rate at the outlet remains constant at 100 g/s, whereas the gas pressure at the inlet remains constant at P_0=0.2 MPa. Based on incompressible conditions and mass conservation, the velocity or flow rate at the inlet can be obtained from that at the outlet. Six monitoring points are set on the sides of the tank, and their locations of the monitoring points are shown in Fig. 6.

3.2.2 Results and Discussion

In this study, three different inlet boundary conditions, namely, the velocity, pressure, and mass flow inlets, are considered to simulate the sloshing of the liquid tank with gas inflow. For each case, the time step is 0.001s, and the total time is 10 s.

Figure 7 shows the distributions of the liquid and gas under three different inlet boundary conditions. It is evident from Fig. 7 (a) and (b) that the velocity and mass flow inlets produced similar liquid distributions in the

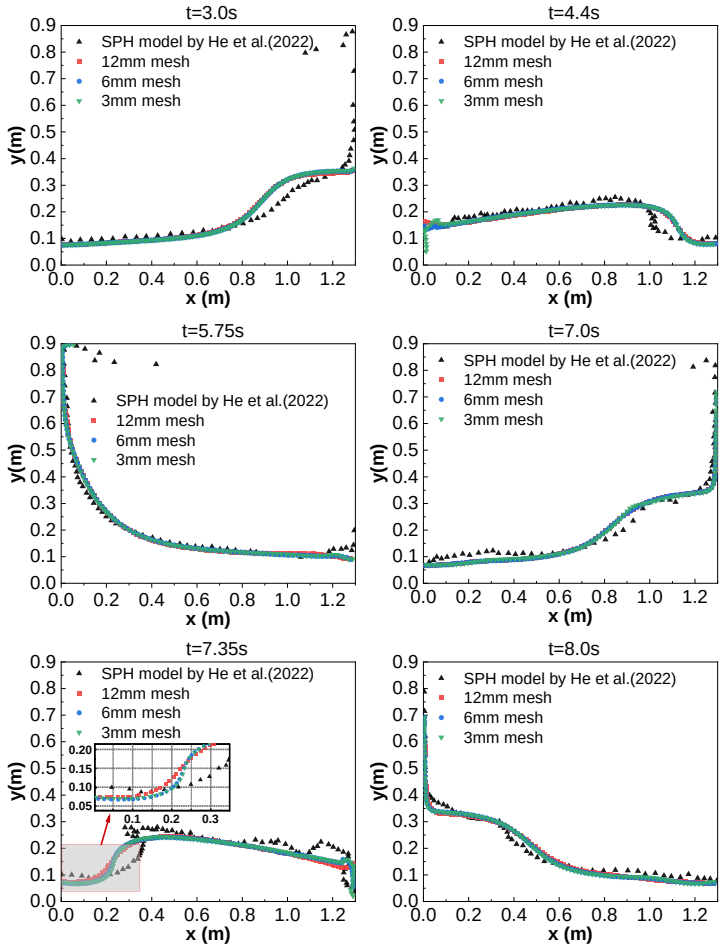

Fig. 4 Profiles of the free surface calculated by FVM and SPH (He et al., 2022)

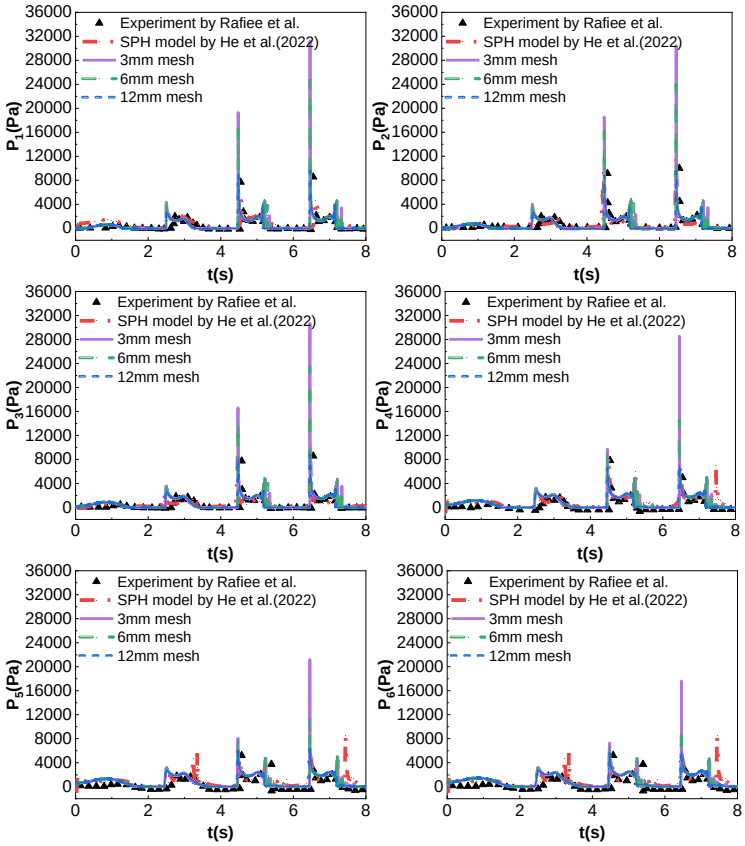

Fig. 5 Time-dependent pressure of the monitoring points via FVM, SPH (He et al., 2022), and experimental data (Rafiee et al., 2011)

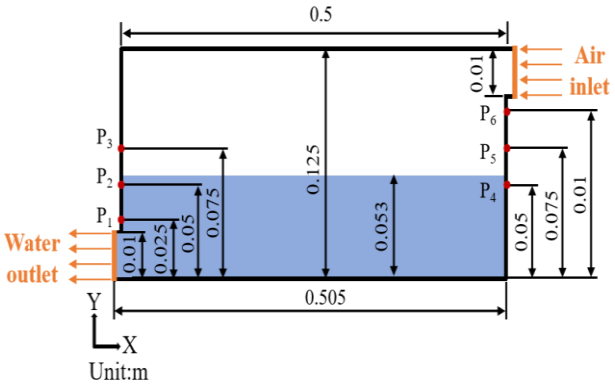

Fig. 6 Computational model of a single liquid tank with gas inflow

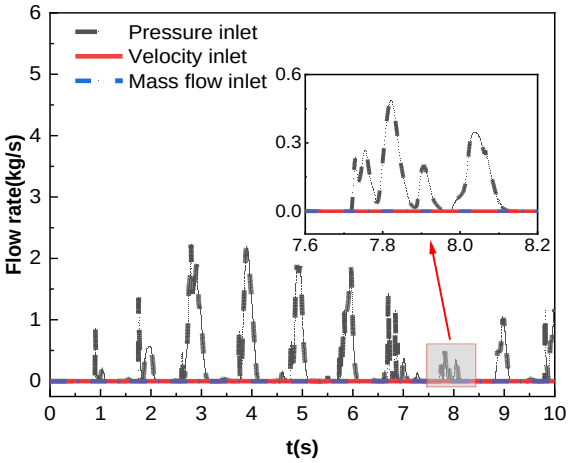

Fig. 8 Flow rates of liquid at the inlet by different inlet boundary conditions

initial stage of sloshing, whereas the pressure inlet shows an evident difference from the other two inlet boundary conditions. As shown in Fig. 8, liquid may flow out from the inlet of the tank when the pressure inlet is selected. The backflow of liquid may cause a pressure imbalance or drop, which can cause serious damage to the engine. Therefore, the pressure inlet is unsuitable for simulating the sloshing of a liquid tank with a gas inflow.

Over time, the velocity and mass flow inlets exhibit noticeable differences owing to the irregularities in liquid splashing, as shown in Fig. 7 (c). However, the flow rates of the liquid from the velocity and mass flow inlets remain constant at zero, indicating that the liquid does not flow out from the inlet of the top tank. To further analyze the velocity and mass flow inlets, Fig. 9 shows the pressure at the monitoring points. Although the pressure curves at the mass inflow inlet are similar to those at the velocity inlet, large and sharp pressure values often occur when the inlet mass flow is selected. Therefore, the velocity inlet is used in the subsequent simulations.

4. SLOSHING OF DUAL LIQUID TANKS WITH GAS INFLOW

4.1 Dual Liquid Tank Model

Figure 10 shows a schematic of the computational model of the dual-liquid tank. The dual liquid tanks have two parts: upper and lower. The upper and lower tanks are connected by a slender pipe with a width of 10 mm and a height of 600 mm. Each tank is rectangular with a width of 500 mm and a height of 125 mm. The blue area represents the liquid, and the blank area represents the gas. The density, dynamic viscosity, and background pressure are the same as those described in Section 3.1. Sinusoidal motion is given by Eq. (20), where the angular frequency ω is 6.28 rad/s. For each case, the time step is 0.001 s, and the total time is 10 s.

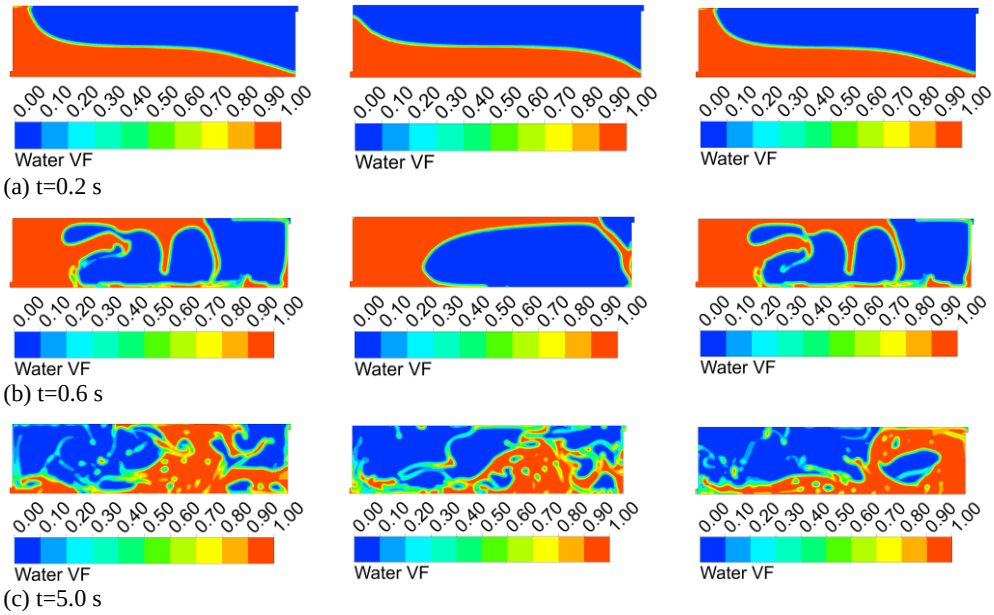

Fig. 7 Distributions of the liquid (red) and gas (blue) under different inlet boundary conditions: (a) t =0.2 s, (b) t =0.6 s, and (c) t =5.0 s. Left: velocity inlet, center: pressure inlet, right: mass flow inlet

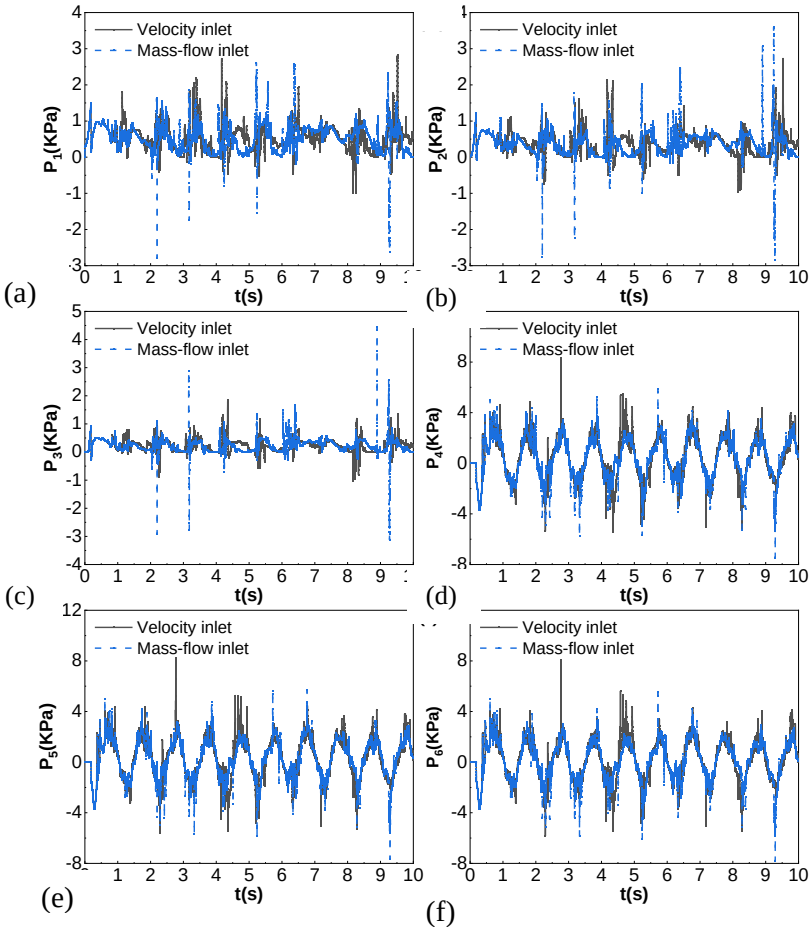

Fig. 9 Time-dependent pressure at the monitoring points by different inlet boundary conditions

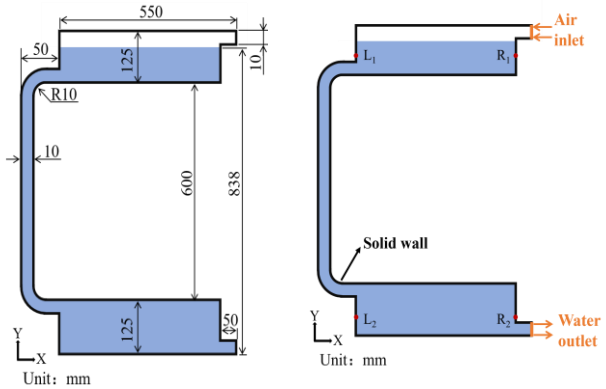

Fig. 10 Schematic diagram of the computational model for the dual liquid tank: (a) dimension schematic and (b) boundary condition schematic

As shown in Fig. 10 (b), four monitoring points (L_1, L_2, R_1, and R_2) are set at the sides of the tanks. The monitoring point L_1 is located at the left side of the upper tank, L_2 is located at the left side of the lower tank, R_1 is located at the right side of the upper tank, and R_2 is located at the right side of the lower tank. The four monitoring points are 748, 42, 748, and 42 mm from the bottom of the lower tank. In this case, three types of boundary conditions exist: inlet, outlet, and solid boundaries. In this study, the inlet boundary is the velocity inlet, the outlet boundary is the mass flow outlet, and the solid boundary is considered to be impenetrable with no-slip walls.

4.2 Effect of Overloads

The initial height of the liquid surface is 838 mm, corresponding to a filling ratio of 99.52%. The flow rate at the outlet is set at 50 g/s. Three different overloads are simulated: A=1G, A=3G, and A=5G, respectively.

Figure 11 shows the distributions of the liquid and gas at various moments under different overload values. Fig. 11 (a) shows that at the beginning of the sloshing, the free surfaces of the liquid gradually become sharp and form a water tongue that rolls toward the right of the tank. Compared to small loads, the front end of the free liquid surface with large loads rolls further. At time t=1 s, for the case A=1G, the liquid is still continuous, and the gas is concentrated in large bubbles; however, for cases with large overloads, the liquid begins to break up, and the gas is dispersed into multiple small bubbles. Figure 11 (c) shows that as the overload increases, the number of small bubbles generate also increases. More violent sloshing can cause greater pressure differences between the gas and liquid, making it more difficult to gather gas into large bubbles. Additionally, the collision and doping effects between the liquid and gas are intensified; thus, the interface between the gas and liquid becomes increasingly blurred.

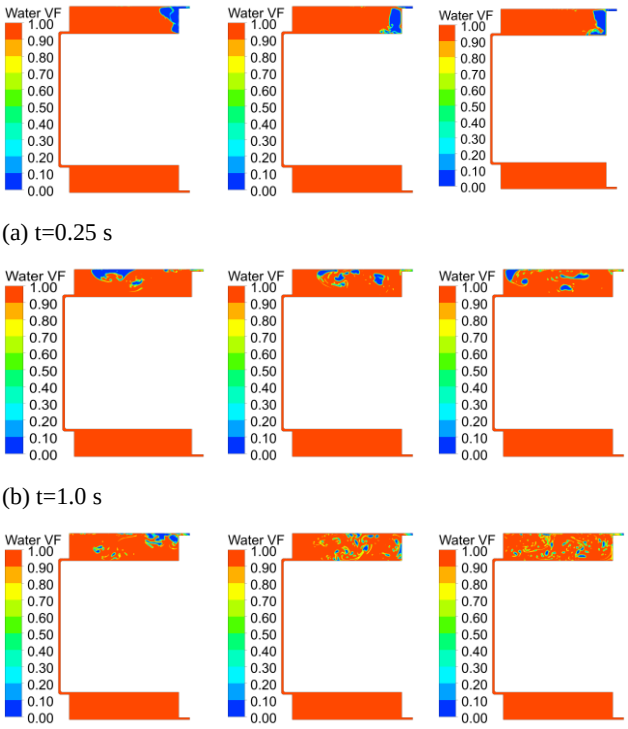

(a) t=0.25 s

(b) t=1.0 s

(c) t=1.5 s

Fig. 11 Distributions of the liquid (red) and gas (blue) at different moments under the different overload values: (a) t=0.25 s, (b) t=1.0 s, and (c) t=1.5 s. Left: *A*=1G, center: *A*=3G, right: *A*=5G

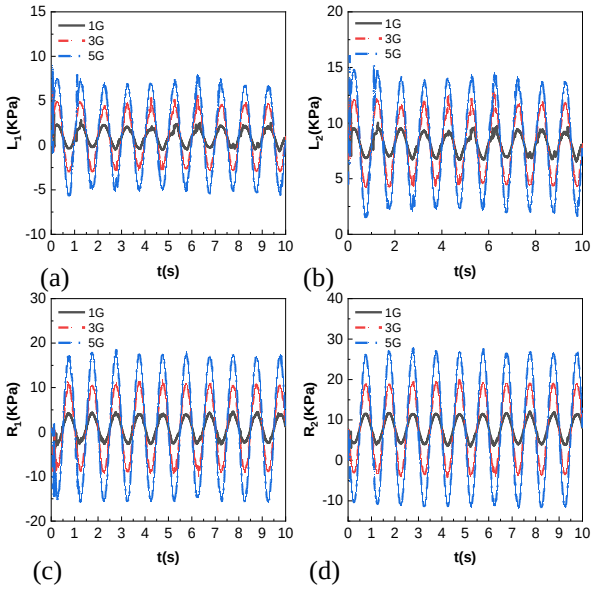

Fig. 12 Time-dependent pressure at the monitoring points under different overloads

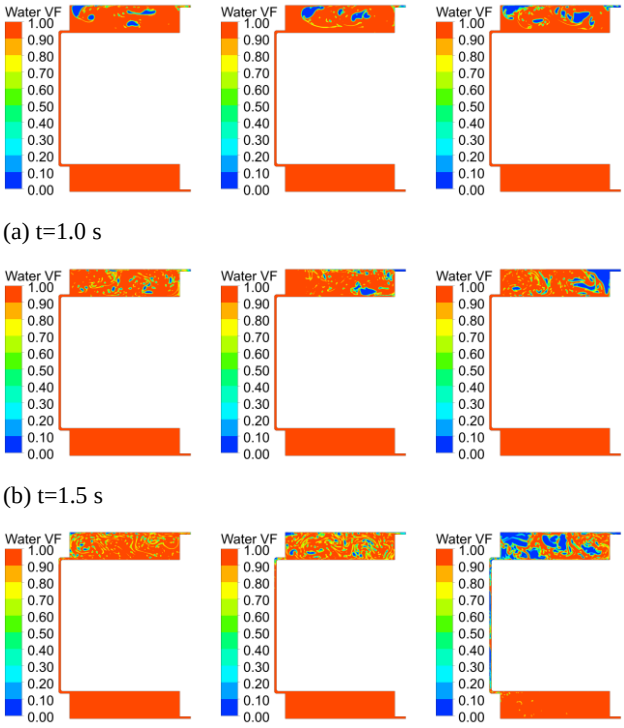

(a) t=1.0 s

(b) t=1.5 s

(c) t=5.0 s

Fig. 13 Distributions of the liquid (red) and gas (blue) at different moments under different outlet flow values: (a) t=1.0 s, (b) t=1.5 s, and (c) t=5.0 s. Left: 50 g/s, center: 1000 g/s, right: 5000 g/s

Figure 12 shows the time-dependent pressures at the monitoring points under different overloads. It can be seen that the pressure shows a periodic oscillation over time and that the amplitude of oscillation increases with the increase of overload. As small bubbles in the liquid phase disturb the flow field, the pressure at the monitoring point is not always smooth. The periodic oscillation of the pressure is consistent with the periodic change in the overload. At the same initial liquid height and frequency, the impact force acting on the wall is positively proportional to the overload, which means that a larger overload causes a larger impact force. Additionally, it can be observed that the peak pressure at monitoring point L_1 is lower than the peak pressure at monitoring point R_1. Similarly, the peak pressure at monitoring point L_2 is lower than that at monitoring point R_2. The pipe on the left side of the tank effectively releases the impact pressure of the liquid acting on the tank wall.

4.3 Effect of Flow Rate at the Outlet

The initial height of the liquid and overload acceleration are 838 mm and 5G, respectively. Three different flow rates are simulated at the outlet: 50, 1000, and 5000 g/s.

Figure 13 shows the distributions of the liquid and gas at different moments under different outlet flows. As shown in Fig. 13 (a), the distributions of the liquid and gas under different flow rates have similar profiles at the beginning of sloshing. Over time, the gas flow into the tank continues to increase, which intensifies the number of bubbles. When the flow rate at the outlet is low, the size of the bubbles caused by the sloshing is also small. However, with an increase in the flow rate at the outlet, the sizes of the bubbles caused by sloshing gradually increases. It is evident from Fig. 13 (c) that the gas is

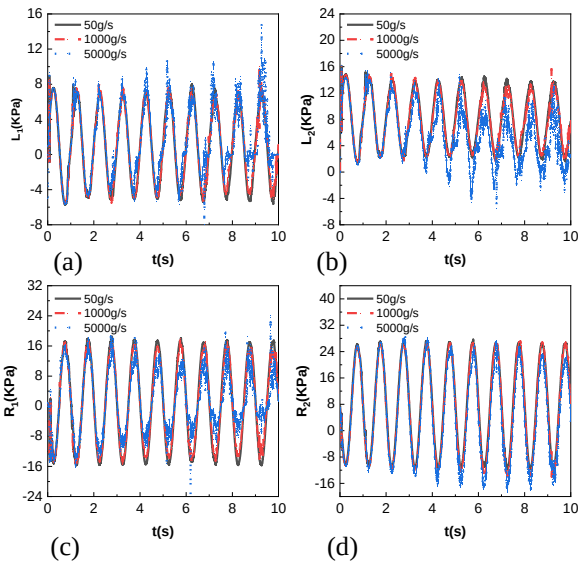

Fig. 14 Time-dependent pressure at the monitoring points under different flow rates

divided into many small bubbles when the flow rate is 50 g/s; the gas is divided into medium-sized bubbles when the flow rate is 1000 g/s; and some large bubbles are observed when the flow rate is 5000 g/s. In particular, when the flow rate is 5000 g/s, the gas flowing into the upper tank increases dramatically, such that some gas flows into the lower tank through the pipe, which could affect the impact force acting on the wall of the lower tank.

Figure 14 shows the time-dependent pressures at the monitoring points under different flow rates. Although the four monitoring points show different peak pressures, the peak pressures of the monitoring points exhibit a similar development trend as the flow rate change. As shown in Fig. 14, the peak pressure exhibits an increasing trend as the flow rate increases, and the pressure curves for low flow rates are smoother than those for high flow rates. The size and number of bubbles play important roles in the impact force acting on the tank wall.

4.4 Effect of Flow Rate of Filling Ratios

The overload acceleration and flow rate at the outlet are 5G and 50 g/s, respectively. Three different initial heights of the liquid surface are simulated: 838, 778, and 748 mm, corresponding to filling ratios of 63.69, 75.64, and 99.52%.

Figure 15 shows the distributions of the liquid and gas at different moments under different filling ratios. When the filling ratio is small, large bubbles are observed, and liquid sloshing is violent. With an increase in the filling ratio, the size of the bubbles gradually decreases, and liquid sloshing tends to be gentle. In particular, when the filling ratio is 63.69%, the gas begins to flow from the upper tank into the pipe at t=1.5 s, affecting the impact force acting on the wall of the lower tank.

Figure 16 shows the time-dependent pressures at the monitoring points for different filling ratios. With an

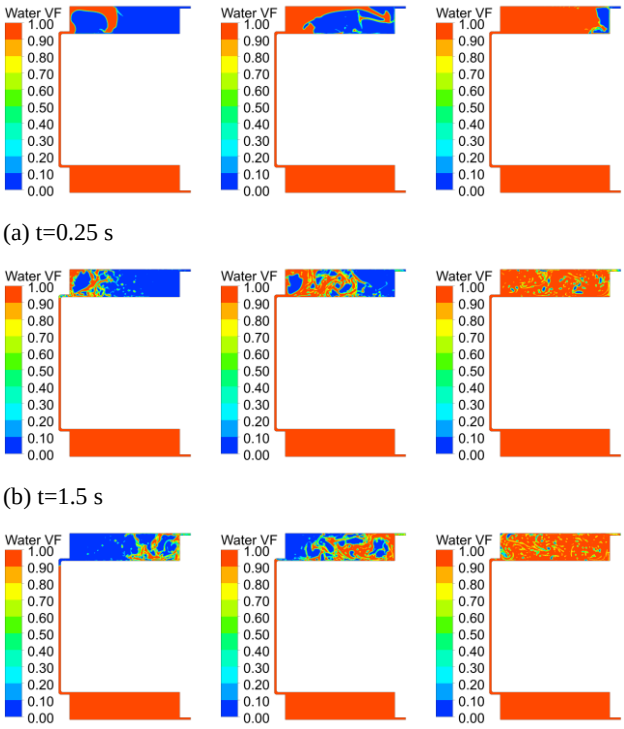

Fig. 15 Distributions of the liquid (red) and gas (blue) at different moments under different filling ratio values: (a) t=0.25 s, (b) t=1.5 s, and (c) t=2.0 s. Left: 63.69%, center: 75.64%, right: 99.52%

increase in the filling ratio, the pressure curves tend to be smooth, and the maximum peak pressure tends to decrease. These results indicate that the size and number of bubbles play important roles in the impact force acting on the tank wall.

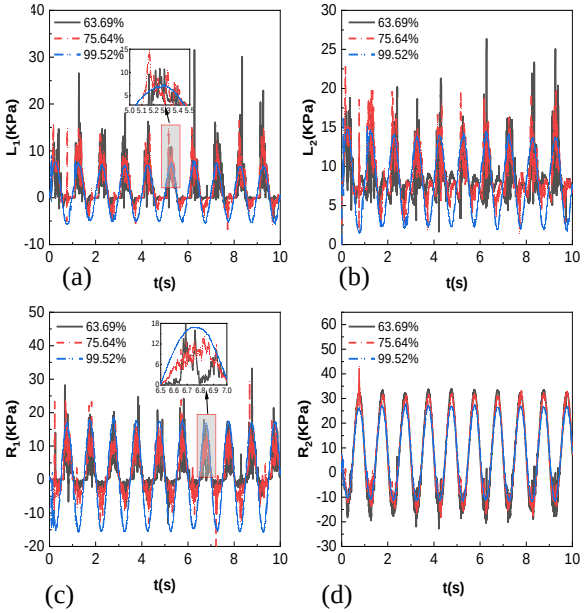

Fig. 16 Time-dependent pressure at the monitoring points under different filling ratios

5. CONCLUSION

In this study, a single-liquid tank sloshing model is numerically simulated to validate the accuracy of the multiphase FVM method. Subsequently, three different inlet boundary conditions are considered, and the velocity inlet is selected. Finally, the multiphase FVM method is used to simulate the sloshing of a dual-liquid tank with gas inflow. The distributions of the liquid and gas and the impact force of the liquid acting on the tank wall are discussed. The following three conclusions can be drawn from a discussion of the numerical results:

1 There is a proportional relationship between the impact force and overload. The inlet and outlet of the pipe release the impact pressure of the liquid acting on the tank wall.

2 With the increase of the flow rate at the outlet, the size and number of bubbles gradually increase. The liquid tends to be violent, the pressure curves tend to be rough, and the maximum peak pressure tends to increase.

3 With an increase in the filling ratio, the size of the bubbles gradually decreases, liquid sloshing tends to be gentle, pressure curves tend to be smooth, and maximum peak pressure tends to decrease.

It is well-known that there is a significant temperature difference between liquid hydrogen and the inflow gas. Therefore, in future studies, it will be necessary to consider the energy equation and discuss the temperature distribution of a sloshing tank with gas inflow. In addition, it is necessary to extend the simulation to three-dimensional spacing and study the three-dimensional flow field of a sloshing tank with gas inflow as well as the effect of the pipe structure on the impact force.

ACKNOWLEDGMENTS

This study has been financially supported by the China Scholarship Council (Grant No. CSC202308110143), National Natural Science Foundation of China (Grant No. 12002002), and Foundation of the North China University of Technology.

CONFLICT OF INTEREST

The author declares no financial or nonfinancial interests in this section. The authors declare that they have no conflicts of interest to disclose.

AUTHORS CONTRIBUTION

Conceptualization, **C. Huang**; Methodology, **Y. F. Chen**; Software, **Y. F. Chen**; Validation, **Y. F. Chen**; Visualization, **Y. F. Chen**; Numerical analysis, **Y. F. Chen** and **C. Huang**; Writing-original draft, **Y. F. Chen**; Writing-Review & Editing, **C. Huang**; Supervision, **C. Huang** and **S. X. Zhang**; Funding acquisition, **W. H. Yan** and **G. P. He** and **S. X. Zhang**.

REFERENCES

Baek, S., Lee, J., Kim, K.-S., Shin, D., Lim, H., Kim, J., Kim, J., Kim, M., Lim, B., Kim, C. h., Han, S., Cho, K., Oh, S., & Ko, J. (2022). Thermal performance evaluation and analysis of helium heat exchanger for cryogenic propellant launch vehicle. *Cryogenics*, *124*. https://doi.org/10.1016/j.cryogenics.2022.103492

Bai, J. L. (2020). *Study of strong nonlinear interaction between wave current and horizontal cylinder* [Doctor's Degree, Shanghai Jiao Tong University]. https://link.oversea.cnki.net/doi/10.27307/d.cnki.gsjtu.2018.000323

Brown, S. A., Ransley, E. J., Zheng, S., Xie, N., Howey, B., & Greaves, D. M. (2020). Development of a fully nonlinear, coupled numerical model for assessment of floating tidal stream concepts. *Ocean Engineering*, *218*. https://doi.org/10.1016/j.oceaneng.2020.108253

Chen, Y., Lu, L. Q., Zhang, J. C., Chen, J., Hu, C. W., & Hu, J. Y. (2023). Establishment and application of equivalent mechanical model for longitudinal sloshing of sprayer tank liquid. *Journal of Agricultural Machinery*, *54*(01), 173–182+195. https://doi.org/10.6041/j.issn.1000-1298.2023.01.017

Dong, Z. (2002). Advances in numerical simulation of three-dimensional water flow. *Journal of Water Resources and Water Transportation Engineering*, *3*(03), 66–73. https://link.oversea.cnki.net/doi/10.16198/j.cnki.1009-640x.2002.03.014

He, F., Zhang, H., Huang, C., & Liu, M. (2022). A stable SPH model with large CFL numbers for multi-phase flows with large density ratios. *Journal of Computational Physics*, *453*. https://doi.org/10.1016/j.jcp.2022.110944.

Hejranfar, K., & Azampour, M. H. (2016). Simulation of 2D fluid–structure interaction in inviscid compressible flows using a cell-vertex central difference finite volume method. *Journal of Fluids and Structures*, *67*, 190–218. https://doi.org/10.1016/j.jfluidstructs.2016.09.009

Huang, X. N., Wang, L., Mao, H. W., Xue, L. J., & Li, Y. Z. (2020). Simulation study on the flow characteristics of cryogenic propellant for rocket lift-off. *Journal of Refrigeration*, *41*(04), 136–143+166. https://doi.org/10.3969/j.issn.0253-4339.2020.04.136

Huang, Y., Q. Deng, J., & Ren, A. L. (2003). Research on lift and drag in unsteady viscous flow around circular cylinders. *Journal of Zhejiang University (Engineering Science)*, *34*(5), 596-601. https://doi.org/10.3785/j.issn.1008-973X.2003.05.021

Ji, X. Y. (2023). *Research on Hydrodynamic Characteristics of Ships with Liquid Tanks under Waves* [Master's Degree, Dalian University of Technology]. https://link.oversea.cnki.net/doi/10.26991/d.cnki.gdllu.2022.001183

Koca, F., & Zabun, M. (2021). Numerical investigation of water sloshing in square tank with multiple baffles. *European Journal of Science and Technology*(28), 1062–1070. https://doi.org/10.31590/ejosat.1012629

Kutlu, A., Uğurlu, B., & Omurtag, M. H. (2017). A combined boundary-finite element procedure for dynamic analysis of plates with fluid and foundation interaction considering free surface effect. *Ocean Engineering*, *145*, 34–43. https://doi.org/10.1016/j.oceaneng.2017.08.052

Li, J. C., Guo, Z. Y., Zhang, Y., Zhao, J. F., Li, K., & Hu, W. R. (2023). Thermal stratification and self-pressurization in a cryogenic propellant storage tank considering capillary effect in low-gravity. *International Journal of Thermal Sciences*, *194*. https://doi.org/10.1016/j.ijthermalsci.2023.108597

Li, Q. F. Chen, B. G., Xie, X. M., Zhong, Y. K., Zheng, X. L., & Bao, R. (2005). Simulation test of natural circulation precooling for cryogenic pump system. *Journal Of Propulsion Technology*, *26*(2), 167-173. https://doi.org/10.3321/j.issn:1001-4055.2005.02.017

Li, Y. L., Zhu, R. C., Miu, G. P., & Fan, J. (2012). Simulation of ship motions coupled with tank sloshing in time domain based on OpenFOAM. *Journal of Ship Mechanics*, *16*(7), 750-758. https://doi.org/10.3969/j.issn.1007-7294.2012.07.004

Liu, F. (2011). *Dynamic analysis of liquid sloshing in storage tanks and research on structural anti-sloshing technology* [Doctor's Degree, Nanjing University of Aeronautics and Astronautics]. https://doi.org/10.7666/d.d167263

Morais, M. V. G. d., Lopez, A. A. O., Martins, J. F., & Pedroso, L. J. (2020). Science - mechanical science; study data from university of brasilia update understanding of mechanical science (Equivalent mechanical model of rectangular container attached to a pendulum compared to experimental data and analytical solution). *Journal of Technology*, *42*(143). https://doi.org/10.1007/s40430-020-2232-7

Rafiee, A., Pistani, F., & Thiagarajan, K. (2011). Study of liquid sloshing: numerical and experimental approach. *Computational Mechanics*, *47*(1), 65–75. https://doi.org/10.1007/s00466-010-0529-6

Saghi, H. (2018). A parametric study on wave–floating storage tank interaction using coupled VOF-FDM method. *Journal of Marine Science and Technology*, *24*(2), 454–465. https://doi.org/10.1007/s00773-018-0564-0

Shao, J. R., Li, H. Q., Liu, G. R., & Liu, M. B. (2012). An improved SPH method for modeling liquid sloshing dynamics. *Computers & Structures*, *100*, 18-26. https://doi.org/10.1016/j.compstruc.2012.02.005

Tsao, W. H., Chen, Y. C., Kees, C. E., & Manuel, L. (2022). The Effect of porous media on wave-induced sloshing in a floating tank. *Applied Sciences*, *12*(11). https://doi.org/10.3390/app12115587

Wan, J. W. (2021). *Numerical solution of finite-volume-based unconfined Navier-Stokes equations and fluid-structure coupling problems by the Lunger-Kutta method* [Doctor's Degree, Southwest Jiaotong University]. https://link.oversea.cnki.net/doi/10.26991/d.cnki.gdllu.2022.001183

Wang, B., Wang, T. X., Huang, Y. H., Wu, J. Y., & Lei, G. (2016). Modeling and pressure control characteristics of thermodynamic venting system in liquid hydrogen storage tank. 67(S2), 20-25. https://doi.org/10.11949/j.issn.0438-1157.20161347

Wang, F. J. (2016). Advances in computational modelling of rotating turbulence in fluid mechanics. *Journal of Agricultural Machinery*, *47*(02), 1–14. https://kns.cnki.net/kcms/detail/11.1964.s.20151130.1722.046.html

Yao, H., Zhang, H., Liu, H., & Jiang, W. (2017). Engineering - Engineering analysis; recent findings from h.l. yao and co-authors provide new insights into engineering analysis (Numerical study of flow-excited noise of a submarine with full appendages considering fluid structure interaction using the boundary element method). *Journal of Engineering*, *77*, 1–9. https://doi.org/10.1016/j.enganabound.2016.12.012

Yu, A. Z. (2021). *Numerical simulation of ship bow wave breaking at high speed* [Master's Degree, Shanghai Jiao Tong University]. https://link.oversea.cnki.net/doi/10.27307/d.cnki.gsjtu.2020.001145

Zeng, Y., Wang, H. B., Sun, M. B., Wang, C., & Liu, X. (2023). SST turbulence model improvements: Review. *Acta Aeronautica et Astronautica Sinica*, *44*(9). https://doi.org/10.7527/S1000-6893.2022.27411

Zhang, Z., Wu, Q., Xie, Y., & Yu, H. (2023a). Experimental and numerical investigations on the liquid tank sloshing in regular waves. *Ocean Engineering*, *271*. https://doi.org/10.1016/j.oceaneng.2023.113668

Zhang, Z. L., Long, T., Chang, J. Z., & Liu, M. B. (2019). A smoothed particle element method (SPEM) for modeling fluid–structure interaction problems with large fluid deformations. *Computer Methods in Applied Mechanics and Engineering*, *356*, 261–293. https://doi.org/10.1016/j.cma.2019.07.024

Zhang, Z. L., Shu, C., Liu, Y. Y., Liu, W., Khalid, M. S., & Ullah. (2023b). An improved M-SPEM for modeling complex hydroelastic fluid-structure interaction problems. *Journal of Computational Physics*, *488*. https://doi.org/10.1016/j.jcp.2023.112233

Zhou, Y., Qian, W. Q., Deng, Y. Q., & Ma, M. S. (2010). Preliminary analysis of parameter effects in the k-ω SST two-equation turbulence model. *Journal of Aerodynamics*, *28*(02), 213–217. https://doi.org/10.3969/j.issn.0258-1825.2010.02.015